Stress chatter on a fracture network reactivated by hydraulic fracturing

A. F. Peña-Castro[1,†], M. P. Roth[2,†], A. Verdecchia[1], J. Onwuemeka[1], Y. Liu[1], R. M. Harrington[2], Y. Zhang[3], H. Kao[4]

[1]Department of Earth and Planetary Sciences, McGill University, Montréal, Québec, Canada
[2]Institute of Geology, Mineralogy and Geophysics, Ruhr University Bochum, Bochum, Germany
[3]School of Earth and Space Sciences, Peking University, China
[4]Pacific Geoscience Centre, Geological Survey of Canada, Sidney, British Columbia, Canada
[†]These authors contributed equally to this work.

Key Points:

- Source parameter inversion and numerical modeling is performed for an M4.5 hydraulic fracturing induced earthquake sequence in northeast BC
- Mainshock is triggered by rapid fluid pressure increase via a hydraulic conduit channeling fluids from injection points to a basement fault
- Most aftershocks are triggered by a static Coulomb stress change resulting from mainshock coseismic slip

Corresponding author: Yajing Liu, `yajing.liu@mcgill.ca`

Abstract

Source processes of injection induced earthquakes involve complex fluid-rock interaction often elusive to regional seismic monitoring. Here we combine observations from a local seismograph array in the Montney Basin, northeast British Columbia, and stress modeling to examine the spatial and temporal evolution of the 30 November 2018 M_L 4.5 hydraulic fracturing induced earthquake sequence. The mainshock occurred at $\sim$ 4.5 km in the crystalline basement two days following injection at $\sim$ 2.5 km, suggesting direct triggering by rapid fluid pressure increase via a high-permeability conduit. Most of the aftershocks are located in the top 2 km sedimentary layers, with focal mechanisms indicating discrete slip along sub-vertical surfaces in a $\sim$ 1 km wide deformation zone. Aftershock distribution is also consistent with static stress triggering from the M_L 4.5 coseismic slip. Our analysis suggests complex hydraulic and stress transfer between fracture/fault networks needs to be considered in induced seismic hazard assessment.

Plain Language Summary

Seismicity linked to hydraulic fracturing (HF) in shale gas exploration in western Canada has increased drastically over the last decade. However, details of induced seismicity sequence evolution and triggering mechanism(s) remain unclear. In this study, we integrate local seismic monitoring and numerical stress modeling for a M_L 4.5 HF induced earthquake sequence in northeast British Columbia, Canada, to reveal a two-step stress transfer process. A nascent, near-vertical fracture network in the sedimentary layers likely developed in the fault growth and basin infill of the Dawson Creek Graben Complex, and hydraulically channeled injected fluids to a thrust fault in the basement, leading to a rapidly increased fluid pressure that initiated the M_L 4.5 mainshock rupture. Static Coulomb stress change from the coseismic slip subsequently triggered the aftershocks along sub-parallel slip surfaces within the overlying sedimentary sequences. Our results also suggest the relative injection volumes and/or wellbore pressures required to create HF at each stage of neighboring wells may be diagnostic of presence of hydraulic connectivity to the basement, which tends to promote larger magnitudes of events.

1 Introduction

Seismicity related to fluid injection in the extraction of unconventional oil and gas resources has increased dramatically in North America in the last decade. While moderate magnitude (M4+) earthquakes in the central and eastern US have been largely attributed to continuous, large-volume wastewater disposal (Ellsworth, 2013), increasing evidence suggests that high-pressure stimulation during hydraulic fracturing is linked to a majority of M3+ earthquakes in the Western Canadian Sedimentary Basin (WCSB) (Atkinson et al., 2016), including several M4+ events in 2015-2019 (Mahani et al., 2017, 2019), posing critical questions as to the triggering mechanisms, seismic hazard assessment and regulatory policies in affected areas. Most of the WCSB M4 earthquakes are inferred to have occurred on pre-existing, unmapped faults in the crystalline basement (Bao & Eaton, 2016; Mahani et al., 2017), yet the stress state of the reactivated faults and their hydraulic connectivity to the injection source region is largely unknown. Remote dynamic triggering studies (Wang et al., 2015) have found evidence of direct and delayed triggering of microseismicity near WCSB injection sites by perturbations of $\sim$ 10 kPa, indicating critically stressed local receiver faults. On the other hand, static stress drop estimates of induced events in WCSB suggest a wide range of values between $\sim$ 0.1 and 100 MPa (Clerc et al., 2016; Zhang et al., 2016; Yu et al., 2019), suggesting a mixture of local stress states, typical of their tectonic counterparts.

Triggering mechanisms proposed to explain the relation between fluid injection and seismicity increase in WCSB mainly involve direct pore pressure increase as fluids migrate in the medium (Bao & Eaton, 2016), or solid matrix stress changes to explain rapid seismic response at distant locations (Deng et al., 2016), or a combination of the two (Yu et al., 2019). However, on a regional scale, only $\sim$ 0.3% of the $\sim$ 12,000 HF wells examined in WCSB (1985-2015) were associated with M3+ earthquakes (Atkinson et al., 2016). On a local scale, some HF wells with relatively larger injection volumes have induced little to no seismicity, whereas significant M4+ events are mainly attributed to wells of moderate injection volumes (Atkinson et al., 2016). These facts raise questions as to how seismic propensity is influenced by local conditions, such as effective hydraulic communication between the injection zones and nearby faults, and the composition and stress state of pre-existing structures. We attempt to address the above questions in this study by combining (1) a source parameter inversion of an M 4.5 HF induced seismic sequence recorded by a local, dense seismograph array and (2) numerical modeling of stress transfer informed by the injection time series.

The gas-bearing Montney Play extends from central Alberta to northeast British Columbia (BC), where conventional oil and gas exploration in the sandstone and dolostone reservoirs has been operating for decades near the foreland limit of the Late Cretaceous-Paleocene Rocky Mountain thrust belt (Figure 1). Located between Fort St. John and Dawson Creek in southern Montney, the Dawson Creek-Septimus area has witnessed a drastic increase in seismicity, from no earthquakes reported by Natural Resources Canada (NRCan) prior to 2013, to a total of $\sim$ 205 cataloged events from 2013-2019 (Fig. S1). With the overarching goal of monitoring seismicity and studying earthquake source processes related to fluid injection in southern Montney, starting in July 2017, McGill University, Geological Survey of Canada (GSC), and BC Oil and Gas Commission (BCOGC) jointly deployed a local dense array consisting of 15 broadband seismic stations in the Dawon Creek-Septimus area (Figure 1). Additional 6 broadband stations were deployed by the Ruhr University Bochum in 2019.

On 30 November 2018 (29 November 2018, local time), a M_L 4.5 earthquake occurred $\sim$ 25 km southeast of Fort St John, northeast BC, the second largest in the Montney Play related to hydraulic fracturing (Mahani et al., 2017). The mainshock was followed by two significant aftershocks of M_L 4.2 and 3.4, leading to the BCOGC's decision to maintain the suspension order of hydraulic fracturing activities at the well pad linked to these events. To our knowledge, this is the first time a complete sequence of a HF induced M_L 4.5 event was captured by a local dense seismograph array, which enables us to determine event source parameters at an unprecedented resolution. Combined with poroelastic stress models informed by injection history at the causal wells, our results reveal a sequential stress transfer process via both fluid-earthquake and earthquake-earthquake interactions, during which the basement fault was reactivated by fluid flow, and possibly aseismic slip along a nascent fracture network in the Dawson Creek graben complex.

2 Earthquake source parameter inversion

2.1 Data and methods

We use waveform data collected at 100Hz at 15 broadband seismic stations, MG01-09 (IRIS network code XL), MONT1-3, MONT6 (network code 1E), and NBC4, NBC7 (network code CN), to invert source parameters of the 30 November 2018 earthquake sequence. Well locations and injection data are reported in the BCOGC database (https://www.bcogc.ca/, last accessed 30 September 2019). A hybrid 1D velocity model (Table S1), where layers above 1 km are from Crust1.0 (Laske et al., 2013) and the deeper layers from (Mahani et al., 2017) is applied in the following data analyses.

For a 20-day period centered at the 30 November 2018 M_L 4.5 mainshock (20 November 2018 to 10 December 2018), an automated Short-Time-Average/Long-Time-Average (STA/LTA) detection employing *SeisComp3* (https://www.seiscomp3.org/) and the *NonLinLoc* location algorithm (Lomax et al., 2000) identified 18 events with M_L 0.8-4.5 (Supplementary Materials). This STA/LTA catalog is further enhanced using a Multi-station Matched-Filter (MMF) method (Chamberlain et al., 2018), which identifies additional events by cross-correlating template waveforms with continuous three-component waveforms at all available stations. Our MMF search with 5 template events (Table S2), including the M_L 4.5 mainshock and its two largest aftershocks, yields a total of 302 events in the 20-day period; 203 detections have at least 4 phase picks for an initial location estimate (Figure 1), with average horizontal/vertical initial *NonLinLoc* location errors of 6.7/4.6 km.

We use two relocation algorithms, *HypoDD* (Waldhauser & Ellsworth, 2000) and *GrowClust* (Trugman & Shearer, 2017), to better constrain the hypocenters of the 203 MMF detections. *HypoDD* results in a total of 68 relocated events and relative horizontal and vertical location errors of 60 and 80 m, respectively. *GrowClust* relocated 59 events, with location errors of 520 m (horizontal) and 450 m (vertical). Both algorithms yield similar relocated hypocenters (Figure 3 and Figure S3). As the travel time residuals are nominally smaller and number of relocated events is slightly larger with *HypoDD* (Figure S4), we will present event locations from this method in the following sections. We use the probabilistic earthquake source inversion framework *Grond* (Heimann et al., 2018) to compute full moment tensors, including non-double couple components, of one foreshock, the M_L 4.5 mainshock, and three aftershocks as listed in Tables S4 and S5. The seismic moment, corner frequency, and static stress drop values of the mainshock and the largest aftershocks are estimated using spectral fitting and used in estimating the radius of the coseismic rupture in Section 3.2. See Supplementary Materials for details of parameter choices in the source parameter analysis. Due to the small magnitudes of most events in the sequence, further improvement in source parameter inversion would require an even denser station coverage near the epicentral area and a high resolution local 3D velocity model.

2.2 Cataloged seismicity and relation to fluid injection

Nearly all the STA/LTA cataloged seismicity in 2018 was spatially correlated with injection well pads, with most intense activity clustered near stations MONT1, MG01, MG03, MG05, and the epicentral area of the M_L 4.5 sequence (Figure 1). However, based on the 2018 seismicity and well distribution, there is no obvious correlation between cumulative injection volume and the number of induced earthquakes or their maximum magnitude. For example, the well located $\sim$ 10 km northeast of MG09 had a total injection volume of 2.5×10^5 m^3 with negligible seismicity detected within a $\sim$ 5 km radius, whereas the two horizontal wells that were stimulated within 15 km of the M_L 4.5 epicenter had only finished a total of 13 ($\sim$ 1.4×10^4 m^3 injected volume) of the 50-60 planned stages before the M_L 4.5 occurred.

The initial locations of the MMF detected events of the 30 November 2018 sequence highlight a primarily northwest-southeast trending structure, which is consistent with the seismicity trend illustrated by the NRCan reported events in this area from 2013-2019 (Fig. S1). Furthermore, the focal mechanism solution of the M_L 4.5 mainshock illustrates a NW-trending focal plane, similar to the August 2015 M_w 4.6 HF induced earthquake $\sim$ 120 km northwest of Fort St. John (Mahani et al., 2017). The thrust-faulting mechanism of both M4.5+ earthquakes suggest that they occurred on pre-existing faults that are optimally oriented in the NE-SW trending maximum regional horizontal stress direction (S_{Hmax}) (Heidbach et al., 2018) (Figure 1).

Figure 2 illustrates the temporal relation between MMF detected seismicity and the per-stage injection volume along two horizontal wells (HW1 and HW2) actively stimulated prior to the M_L 4.5 sequence. Of the 302 detections, 32 occurred prior to the first stage of HW1, with the largest being an M_L of 1.36; 41 occurred during the combined 13 stages (the last stage ended 12 minutes before the origin time of the M_L 4.5 mainshock) with the largest being an M_L of 2.11; 147 occurred in the 48 hours following the mainshock, and 82 occurred in the subsequent days (until 10 December 2018). Most of the seismic moment was released within one hour by the mainshock and two largest aftershocks. The cumulative injection volume of the 13 completed stages is $\sim 1.4 \times 10^4$ m^3, an order of magnitude lower than that predicted by the inferred linear relationship between the maximum magnitude and total injection volume (McGarr, 2014). The persistent deviation from the injection volume-maximum magnitude relation reported for several HF induced M4+ earthquakes in the WCSB (Atkinson et al., 2016) suggests that they may have distinct source mechanisms from those induced by wastewater disposal and enhanced geothermal stimulation.

2.3 Relocated seismicity and inferred fracture network

Figure 3 shows that most of the relocated events cluster around the terminus of the horizontal wells, demonstrating a clear spatial coincidence to the stages stimulated prior to the mainshock. The clear spatiotemporal proximity between injection and seismicity (Figures 2 and 3) indicates that stimulation at HW1 and HW2 are most likely the direct cause of this M_L 4.5 sequence. The fault plane solutions of the M_L 4.5 mainshock and its three largest aftershocks (M_L 4.2, 3.6 and 2.8) exhibit a mix of thrust and strike-slip kinematics, suggesting both types of reactivated slip surfaces are approximately optimally oriented in the regional stress field, and that the two least compressive stresses of the local ambient stress field may be close in magnitude.

Except for the M_L 4.5 mainshock and a few other events relocated in the crystalline basement, nearly all relocated earthquakes are in the upper $\sim$ 2.5 km of sedimentary layers above the horizontal wells drilled through the Lower Montney formation, and exhibit a sub-vertical distribution (Figure 3c and 3d). We interpret the near-vertical structure defined by relocated seismicity and primarily strike-slip fault plane solutions of three largest aftershocks as a nascent fault zone in which deformation has yet to accumulate to create a through-going planar slip surface. The width of the deformation zone is $\sim$ 1 km as suggested by hypocenters with *HypoDD* horizontal/vertical relocation errors of 60/80 m. Such a relatively immature fault zone may evolve through the linkage of distributed deformation bands as deformation progresses, similar to fault zone growth documented in sedimentary rocks in Utah (Shipton & Cowie, 2001). Although the seismicity distribution suggests a limited fault interaction between the basement fault on which the M_L 4.5 mainshock occurred and the presumed fault network in the overlying sedimentary layers, their spatial clustering and temporal correlation with the injection time history at HW1 and HW2 indicates an effective stress transfer process between the two fault systems.

3 Numerical modeling of stress transfer

3.1 Poroelastic stress model

As the mainshock occurred within two days from the onset of injection, but at a distance of over 2 km from the injection depth, we hypothesize that a highly permeable conduit may have facilitated fluid transport from the injection sources to the mainshock fault, hence rapidly increased the pore pressure on the fault within 1-2 days, which was sufficient to trigger the mainshock. To test the hypothesis, we develop a poroelastic stress model using the finite element software *Comsol Multiphysics*® following a linear poroelasticity framework (Biot, 1941). Two high-permeability zones are embedded in the model domain: a vertical conduit allowing fast fluid migration from the injection depth to the basement, and a damage zone flanking the mainshock fault plane, with orientation inferred from its focal mechanism solution (Figure 3b). See Supplemental Materials for model parameter details. Using the injection time series along HW1 and HW2 (Figure 2) and assuming a permeability contrast of 10^{-12} m^2 within the conduit zones and 10^{-16}-10^{-19} m^2 within the country rock, pore pressure at the mainshock hypocenter effectively increases by ~ 0.1 MPa, which is $\sim$ 1-2 orders of magnitude higher than the stress perturbations associated with dynamic triggering of seismicity in WCSB (Wang et al., 2015, 2019). Without such high-permeability conduits, inferred pore pressure and poroelastic shear/normal stress changes on the mainshock fault are negligible in amplitude (1.5×10^{-4} MPa) within two days of injection onset (Figure S8). Such stress perturbations are significantly lower than previously observed dynamic triggering thresholds (Wang et al., 2015, 2019), rendering the physical model with conduits as being more plausible.

3.2 Coulomb stress model

Next, we use *Coulomb* 3.3 (Toda et al., 2011) to calculate the Coulomb stress change $\Delta CFS = \Delta\tau - \mu(\Delta\sigma + \Delta p)$ due to the coseismic slip from the mainshock, resolved onto a receiver fault plane following the kinematics (strike, slip, rake) of the largest aftershock (M_L 4.2) (Table S4). Here, $\Delta\tau$ is the change in shear stress (positive in the direction of the receiver fault slip), μ is the friction coefficient, $\Delta\sigma$ is the change in normal stress (positive when the receiver fault is unclamped), and Δp is the pore pressure change. We assume the coseismic slip is uniformly distributed on a circular crack with a radius constrained by the mainshock corner frequency estimate and the seismic moment estimated from the moment tensor solution (Supplementary Materials, Figures S5-S7). As shown in Figures 3c and 3d, except for a single event that does not cluster around the stimulated stages, all the relocated aftershocks are distributed within the positive Coulomb stress regime, strongly suggesting the continuation of the sequence by earthquake-earthquake interaction via static Coulomb stress triggering. We also conduct a finite slip inversion of the M_L 4.5 mainshock using all the 15 stations (Supplementary Materials). Despite the more heterogeneous slip distribution over a broader area and hence smaller amplitudes of Coulomb stress changes, nearly all aftershocks are still located within the positive Coulomb stress regime (Figure S10).

4 Discussion

4.1 Two-step stress transfer

The relative offset between the injection depth and the M_L 4.5 hypocenter suggests that while the initial stress perturbation to induce larger magnitude earthquakes may have resulted from injection activity, the interaction between natural fault systems in the basement and the overlying sedimentary layers dictates the seismicity evolution. The focal mechanism solution of the mainshock suggests that its orientation in the regional stress field is optimal for reactivation, thus, the long term deformation history may have simply been time-advanced through the pressure perturbation from injection. The roughly east-west trend of the nodal and fault planes depicted in Figures 3a and 3b are also consistent with the general trend of the Dawson Creek Graben Complex, and the estimated $\sim 50^\circ$ dip angle is consistent with a normal fault that has been reactivated in the present-day ambient stress field (Barclay et al., 1990). The spatially diffuse distribution of aftershocks suggests a network of unconnected slip surfaces, such as those documented in young (low cumulative offset) fault systems that form in porous sedimentary rocks (Shipton & Cowie, 2001). Fault growth begins in such sedimentary rocks with short segments of slip surfaces that eventually link up as deformation accumulates, where remaining unconnected surfaces grow into a damage zone with continued deformation (Shipton & Cowie, 2001). The distribution of aftershocks directly above the mainshock fault would be a seismic indicator of the presence of such a nascent fault system that likely formed during synchronous basin infill with graben formation, and likely functioned as a high-permeability pathway to funnel fluids to the mainshock fault. The separation between the mainshock slip surface and the aftershock zone may suggest that the proposed graben fault and sub-vertical fracture network do not yet have an intersecting slip surface. However, interacting faults are not required to be geometrically or kinematically linked to transfer stress, but rather, can interact through overlapping damage, or strain fields (Trudgill & Cartwright, 1994; Peacock et al., 2017).

Figure 4 provides a conceptual framework for the coeval formation of the subsurface structure consistent with the observations and numerical modeling results presented here. As the initial tectonic regime during graben formation was extensional, sediment infill began, and the progressive growth of the graben may have caused strain accumulation along a zone of weakness in the overlying sediments, where a diffuse network of slip surfaces formed as basin infill continued to accumulate (shown as the vertical column of black lines cutting through the dolostones and limestones in Figure 4). The oldest dolostone and limestone sediments of the Debolt formation adjacent to the basement would have experienced the most cumulative offset, and thus would be expected to have the most extensively developed fracture network relative to the younger sedimentary layers deposited above (Barclay et al., 1990). Due to the low regional deformation rate (Kao et al., 2018), the cumulative offset in the weak zone extending from the basement contact to the surface would possibly be low enough to prevent a through-going slip surface to form within. As cumulative offset should correlate with fracture network density, the latter would also be expected to gradually decrease toward the surface to negligible values. The fracture network also correlates with permeability, which is also expected to increase with the age of sediments, and hence better facilitate fluid transport at greater depth (Caine et al., 1996). Once the mainshock is triggered by the fluids traveling from the injection points to the basement fault, the fracture network provides a zone of weakness susceptible to further triggering via the Coulomb stress perturbation from the static offset of the mainshock. The Coulomb stress triggering mechanism would also be consistent with the dearth of aftershocks observed in the stress shadow directly above the mainshock (Figure 3d), where the negative Coulomb stress change could function to clamp fractures closed directly outside the focal volume (in the dolostone and limestone layer).

The lack of seismicity in the dolostone and limestone layer could also be manifestation of effective fault strengthening as fluids migrate downward through the fracture network, where porosity development in the dolomitization process would favor strong dilatancy, a mechanism that has been shown to inhibit dynamic deformation in landslides, glacier tills, and fault gouges (Marone et al., 1990; Moore & Iverson, 2002), and leads to aseismic slip in various tectonic settings (Segall et al., 2010; Liu, 2013). Stress loading from aseismic creep has been proposed as an alternative mechanism for triggering earthquakes under fluid injection (Bhattacharya & Viesca, 2019; Cappa et al., 2019), in particular for events that occur at spatial and temporal scales unfavorable for fluid diffusion or poroelastic stress triggering (Eyre et al., 2019). In our model, pore pressure increases by 0.1 MPa on the mainshock fault within 2 days of injection onset when permeability in the near-vertical conduit is assumed to be 10^{-12} m^2; a lower permeability of 10^{-13} m^2 would result in a pore pressure increase of ~ 0.001 MPa for the same time scale. Our proposed model is thus more compatible with a combined loading effect from fluid diffusion and possible aseismic creep along the near-vertical fracture network.

The well treatment in the Upper Montney formation in May 2018 also induced a similar number of events, compared with the November sequence (17 vs. 20), based on our automated STA/LTA catalog, although the sequence in May had a maximum magnitude of M_L 2.3 and there were no felt reports. While the fracture network depicted in Figure 4 likely extends through the well bores used for the May 2018 treatment in the Upper Montney formation, we infer that the hydraulic communication from the Upper Montney to the basement fault must not have existed, otherwise the larger injection volume and longer injection period in May may have triggered M_L 4+ event(s) prior to the treatment of the Lower Montney in November.

4.2 Implications for seismic hazard and regulation

The HF process requires building up downhole pressures to values roughly equal to or greater than the magnitude of the least compressive stress (σ_3) in order to initiate fractures. It has been hypothesized that the fracturing process may be less effective for wells hydraulically connected to well developed, pre-existing basement fault systems (Kozłowska et al., 2018), similar to the case suggested in our conceptual model (Figure 4). Fault conduit behavior, particularly in crystalline (basement) rocks, could funnel fluids away from the volume of the target reservoir, and provide an explanation for cases (Atkinson et al., 2016), including this study, where the inferred injection volume-maximum magnitude relationship (McGarr, 2014) does not hold.

Multiple lines of evidence are in general consistent with the above reasoning. Based on the per-stage injection volume reported by BCOGC, injection into the Lower Montney formation associated with the November 2018 M_L 4.5 required over twice volume per stage of fluid for the HF process when compared with horizontal wells stimulated directly above ($\sim$ 300 m) in the Upper Montney from the same vertical well pad in May 2018. The average injection volume required for the May treatment in the Upper Montney formation was 544 m^3 per stage compared with 1,190 m^3 per stage for HW1 and HW2 in the Lower Montney. If we assume that the pressure needed to overcome the regional σ_3 is the same in the wells located in the two formations separated in depth only by 300 m, it implies that larger volumes of HF fluid were needed in comparable rock volumes to achieve the same downhole pressure in the Lower Montney. The most plausible explanation for the difference in the required fluid volume is that fluid is being lost while or shortly after pumping activity attempts to drive pressure up, which is consistent the conceptual model of the fracture network conduit (Figure 4) funneling fluids to the basement fault via the two intersecting damage zones.

The fluid conduit model proposed here is also consistent with the relatively low, $\sim$ 50%, flowback rate for WCSB HF wells reported by BCOGC and in Alberta (Bao & Eaton, 2016), which implies that more than half of the injected fluids remain in the subsurface and likely contribute to the sustained pressurization of existing fault zones connected to fluid pathways. A similar spatial pattern of larger magnitude events occurring in the basement while nearly all aftershocks in the sedimentary layers has been observed at HF wells near the Crooked Lake, Alberta, where one of the wells associated with an M_w 3.9 reported a flowback rate of merely $\sim$ 7% (Bao & Eaton, 2016). Although on a broad, regional scale HF injection volume has been shown to correlate with the frequency of earthquakes in the Duvernay formation, Alberta (Schultz et al., 2018), observations presented in this study suggest a possible relation to the relative magnitude, if examined across nearby wells. Industrial operators often have real-time information regarding relative volumes needed to reach overpressure levels at neighboring wells. If certain wells require higher volumes of fluids compared to nearby wells to reach overpressure levels, it could serve as an effective diagnostic tool to identify possible presence of faults hydraulically connected to the injection sources, and ultimately, help avoid inducing large magnitude events.

5 Conclusions

In this study, we combined seismic observations and numerical stress modeling to investigate the source processes of an M_L 4.5 (30 November 2018) hydraulic fracturing (HF) induced earthquake sequence in the Dawson Creek-Septimus area of the Montney Basin, British Columbia. This event was the second largest HF induced earthquake in BC, and the first detected by a local dense seismic array. For a 20-day period centered at the mainshock origin time, we enhanced the automatic STA/LTA catalog by a multi-station matched-filter (MMF) method. The MMF catalog consists of a total of 302 detections, out of which 203 have initial location solutions and 68 were relocated. The M_L 4.5 mainshock occurred at a depth of $\sim$ 4.5 km in the crystalline basement, about two days following the onset of injection at $\sim$ 2.5 km along two nearby horizontal wells. The large spatial but short temporal separation between the onset of injection and the occurrence of the mainshock suggests direct triggering by rapid fluid pressure increase via a high-permeability conduit connecting the two sources, which we confirmed with poroelastic stress modeling. The presence of such a hydraulic conduit is also supported by the much higher per stage injection volumes required to initiate HF in the Lower Montney than those in the Upper Montney layer $\sim$ 300 m above.

Relocated aftershocks are mainly in the top 2 km sedimentary layers, with predominantly strike-slip focal mechanisms indicating discrete slip along sub-vertical surfaces in a $\sim$ 1 km wide deformation zone. The deformation zone likely represents a nascent, near-vertical fracture network developed in the fault growth and basin infill of the Dawson Creek graben complex, and serves as a hydraulic conduit channeling fluids to the thrust fault in the basement, where the M_L 4.5 mainshock ruptured. Coulomb stress model suggests that most of the aftershocks were triggered by the static stress transfer from the M_L 4.5 coseismic slip. Our results also suggest that the relative injection volumes and/or well bore pressures at each HF stage of neighboring wells may be diagnostic of the presence of hydraulic connectivity to the crystalline basement, therefore a possible monitoring strategy for preventing large magnitude of events.

Acknowledgments

This study was supported by Natural Sciences and Engineering Research Council of Canada Strategic Grant STPGP/494141-2016, Deutsche Forschungsgemeinschaft Grant 428868223, and partially by an Natural Resources Canada (NRCan) Energy Innovation grant and

BC Oil and Gas Commission (BCOGC). We thank Stuart Venables and BCOGC staff for coordinating field logistics and communication with partners. Field deployment trips were led by Greg Langston (McGill) with contributions from NRCan, BCOGC and the RUB. Waveform data used in this study is archived at IRIS under network codes XL, 1E and CN (e.g., http://ds.iris.edu/gmap/XL).

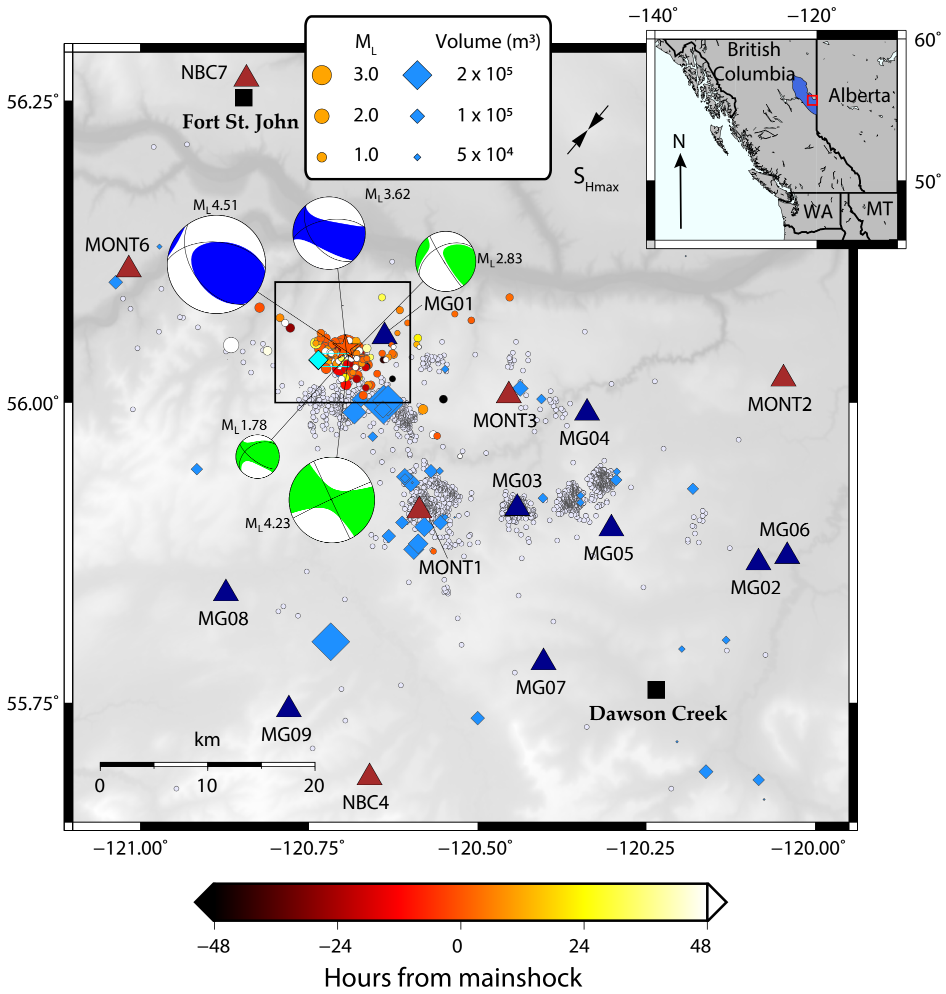

Figure 1. Earthquakes, seismic station, and hydraulic fracturing well distributions in the Dawson-Septimus area, northeast BC. Colored circles are MMF detected and located events 48 hours before and after the M$_L$4.5 mainshock. MMF detections outside this period are colored in black (before) and white (after). Grey dots are STA/LTA detections January to December 2018. Blue diamonds are active HF wells in 2018 scaled by injection volume. Cyan diamond shows the well pad from which injection along two horizontal wells immediately preceded the M$_L$4.5 event. S_{Hmax} represents regional maximum horizontal stress. The blue area in the inset shows the areal extension of the Montney Play in BC.

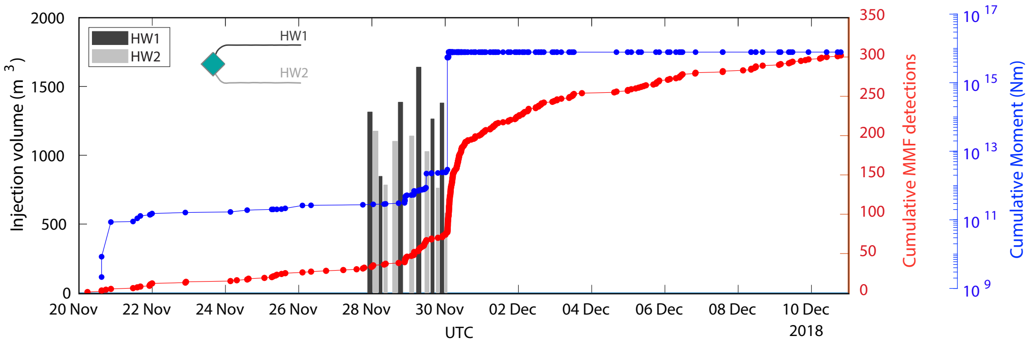

Figure 2. MMF-deteced seismicity (red) and injection volume per stage (gray and black bars) along the two horizontal wells stimulated before the occurrence of the M_L4.5. No other wells were stimulated within 15 km of the epicenter during this period. Cumulative seismic moment shown in blue.

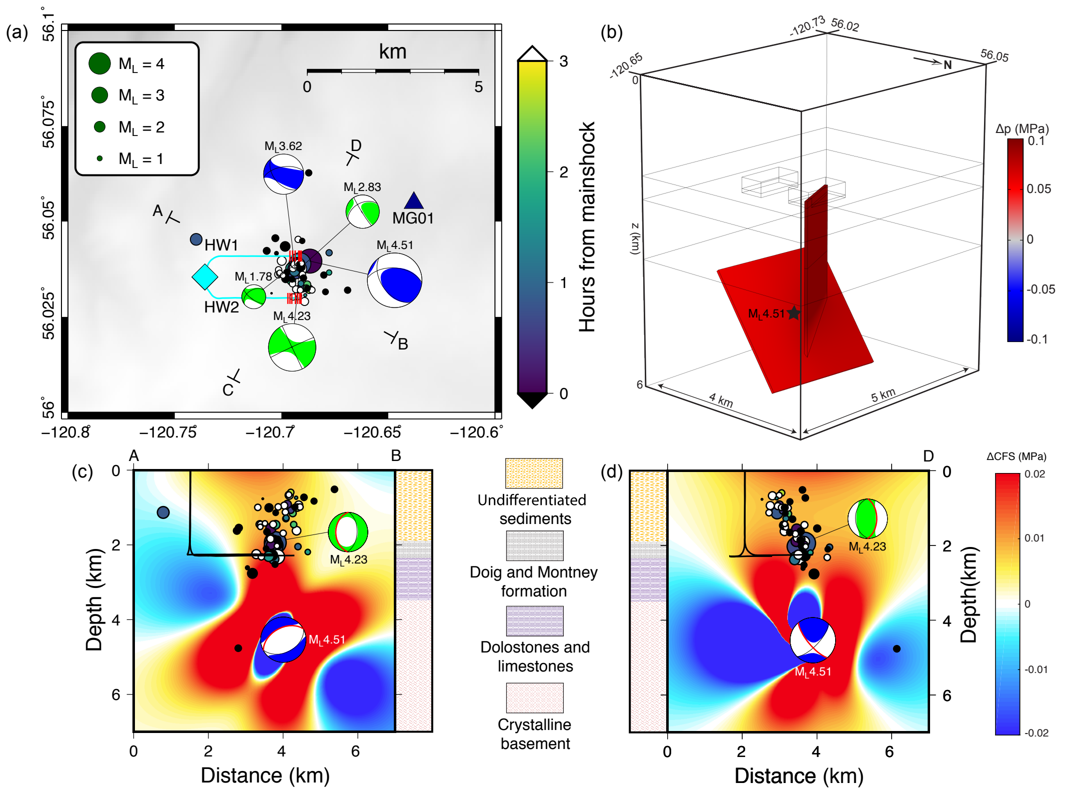

Figure 3. Relocated seismicity and Coulomb stress changes. (a) Map view of 68 earthquakes relocated with hypoDD, and focal mechanism solutions of the M_L4.5 mainshock and four aftershocks. Red lines perpendicular to HF wells HW1 and HW2 trajectories depict the stages completed before the M_L4.5. (b) Pore pressure change Δp due to injection history along HW1 and HW2 as in Fig. 2. Permeability of $k = 10^{-12}\mathrm{m}^2$ is assumed along both the mainshock fault plane and a vertical conduit connecting the injection points to the mainshock fault. $k = 10^{-16}$-$10^{-19}\mathrm{m}^2$ elsewhere in the model domain. See Methods for details. (c) and (d) Static Coulomb stress changes due to the coseismic slip of the mainshock, assuming a circular slip area under a static stress drop of 5.3 MPa (Methods and Supplement Information). Receiver fault kinematics (strike 245°, dip 88°, rake 0.4°) follow the focal mechanism solution of the largest (M_L4.2) aftershock.

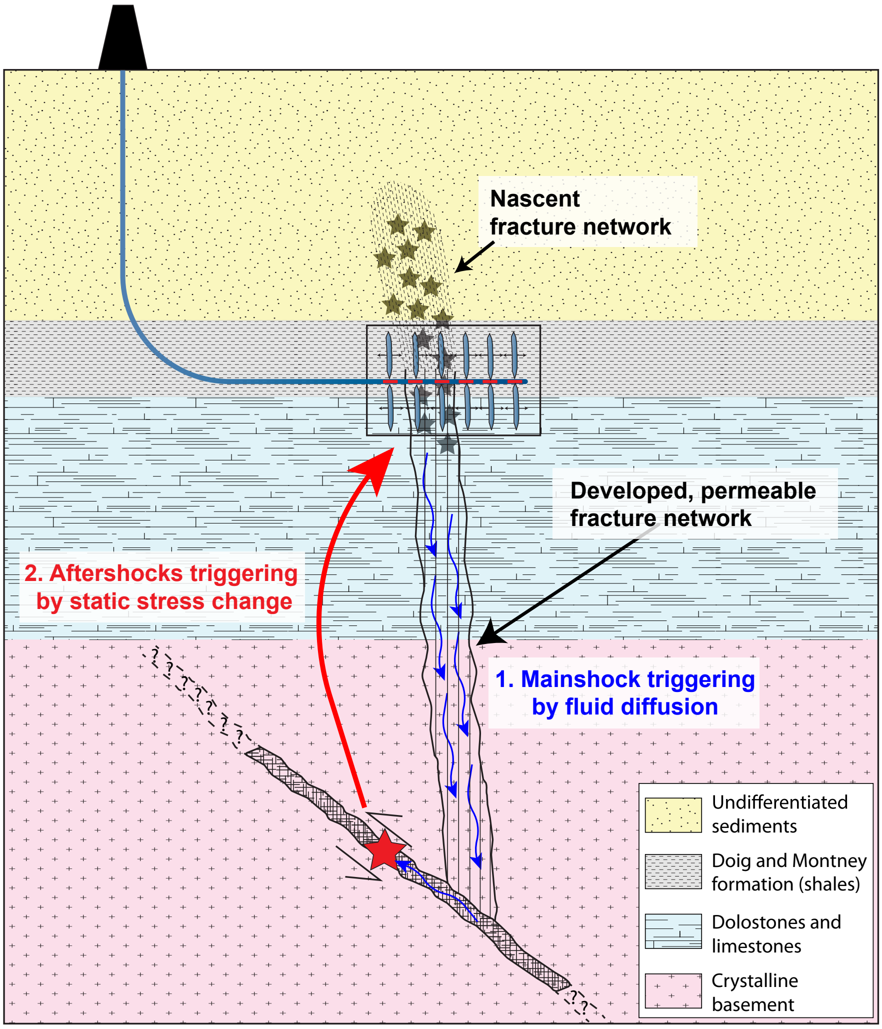

Figure 4. Conceptual diagram showing the two-step stress transfer during and shortly after HF stages. Injected fluid migrates (blue arrows) vertically through a developed, permeable fracture network to the basement fault and pore pressure increase triggers the mainshock (red star) fault plane. Static Coulumb stress changes due to the mainshock coseismic slip subsequently trigger aftershocks along a nascent fracture zone in the sedimentary layers.

References

Atkinson, G., Eaton, D. W., Ghofrani, H., Walker, D., Cheadle, B., Schultz, R., ... Kao, H. (2016). Hydraulic fracturing and seismicity in the Western Canada Sedimentary Basin. *Seismological Research Letters*, *87*, 631-647.

Bao, X., & Eaton, D. W. (2016). Fault activation by hydraulic fracturing in Western Canada. *Science*, *354*, 1406–1409. doi: 10.1126/science.aag2583

Barclay, J., Krause, F., Campbell, R., & Utting, J. (1990). Dynamic casting and growth faulting: Dawson Creek graben complex, Carboniferous-Permian Peace River embayment, Western Canada. *Bulletin of Canadian Petroleum Geology*, *38*(1), 115–145.

Bhattacharya, P., & Viesca, R. C. (2019). Fluid induced aseismic fault slip outpaces pore fluid migration. *Science*, *364*.

Biot, M. (1941). General three-dimensional theory of poroelasticity. *J. Appl. Phys*, *12*, 155–164.

Caine, J. S., Evans, J. P., & Forster, C. B. (1996). Fault zone architecture and permeability structure. *Geology*, *24*(11), 1025–1028.

Cappa, F., Scuderi, M. M., Collettini, C., Guglielmi, Y., & Avouac, J.-P. (2019). Stabilization of fault slip by fluid injection in the laboratory and in situ. *Science Advances*, *5*.

Chamberlain, C. J., Hopp, C. J., Boese, C. M., Warren-Smith, E., Chambers, D., Chu, S. X., ... Townend, J. (2018). EQcorrscan: Repeating and near-repeating earthquake detection and analysis in Python. *Seismological Research Letters*, *89*(1), 173–181.

Clerc, F., Harrington, R. M., & Liu, Y. (2016). Stress drop estimates and hypocenter relocations of induced seismicity near Crooked Lake, Alberta. *Geophys. Res. Lett.*, *43*, 6942–6951.

Deng, K., Liu, Y., & Harrington, R. M. (2016). Poroelastic stress triggering of the December 2013 Crooked Lake, Alberta, induced seismicity sequence. *Geophysical Research Letters*, *43*(16), 8482–8491.

Ellsworth, W. L. (2013). Injection-induced earthquakes. *Science*, *341*, 1225942-1225942. doi: 10.1126/science.1225942

Eyre, T. S., Eaton, D. W., Garagash, D. I., Zecevic, M., Venieri, M., Weir, R., & Lawton, D. C. (2019). The role of aseismic slip in hydraulic fracturing induced seismicity. *Science Advances*, *5*.

Heidbach, O., Rajabi, M., Cui, X., Fuchs, K., Müller, B., Reinecker, J., ... Zoback, M. (2018). The world stress map database release 2016: Crustal stress pattern across scales. *Tectonophysics*, *744*, 484 – 498. doi: https://doi.org/10.1016/j.tecto.2018.07.007

Heimann, S., Isken, M., Kühn, D., Sudhaus, H., Steinberg, A., Vasyura-Bathke, H., ... Dahm, T. (2018). *Grond - A probabilistic earthquake source inversion framework.* Retrieved 2018-08-27, from `http://pyrocko.org/grond/docs/current/` doi: 10.5880/GFZ.2.1.2018.003

Kao, H., Hyndman, R., Jiang, Y., Visser, R., Smith, B., Mahani, A. B., ... He, J. (2018). Induced seismicity in Western Canada linked to tectonic strain rate: implications for regional seismic hazard. *Geophysical Research Letters*, *45*, 11104-11115.

Kozłowska, M., Brudzinski, M. R., Friberg, P., Skoumal, R. J., Baxter, N. D., & Currie, B. S. (2018). Maturity of nearby faults influences seismic hazard from hydraulic fracturing. *Proceedings of the National Academy of Sciences*, *115*(8), E1720–E1729.

Laske, G., Masters, G., Ma, Z., & Pasyanos, M. (2013). Update on crust1. 0—a 1-degree global model of earth's crust. In *Geophys. res. abstr* (Vol. 15, p. 2658).

Liu, Y. J. (2013). Numerical simulations on megathrust rupture stabilized under strong dilatancy strengthening in slow slip region. *Geophys. Res. Lett.*, *40*, 1311–1316. doi: 10.1002/grl.50298

Lomax, A., Virieux, J., Volant, P., & Berge-Thierry, C. (2000). Probabilistic earthquake location in 3D and layered models. In *Advances in seismic event location* (pp. 101–134). Springer.

Mahani, A. B., Kao, H., Atkinson, G. M., Assatourianas, K., Addo, K., & Liu, Y. (2019). Ground motion characteristics of the 30 November 2018 injection induced earthquake sequence in northeast British Columbia, Canada. *Seismological Research Letters*, *90*(4), 1457-1467.

Mahani, A. B., Schultz, R., Kao, H., Walker, D., Johnson, J., & Salas, C. (2017). Fluid injection and seismic activity in the Northern Montney Play, British Columbia, Canada, with special reference to the 17 August 2015 Mw 4.6 induced earthquake. *Bulletin of the Seismological Society of America*, *107*(2), 542-552. doi: 10.1785/0120160175

Marone, C., Raleigh, C. B., & Scholz, C. H. (1990). Frictional behavior and constitutive modeling of simulated fault gouge. *J. Geophys. Res*, *95*(B5), 7007–7025.

McGarr, A. (2014). Maximum magnitude earthquakes induced by fluid injection. *J. Geophys. Res.*, *119*, 1008-1019. doi: 10.1002/2013JB010597

Moore, P. L., & Iverson, N. R. (2002). Slow episodic shear of granular materials regulated by dilatant strengthening. *Geology*, *30*, 843–846.

Peacock, D., Dimmen, V., Rotevatn, A., & Sanderson, D. (2017). A broader classification of damage zones. *Journal of Structural Geology*, *102*, 179–192.

Schultz, R., Atkinson, G., Eaton, D. W., Gu, Y. J., & Kao, H. (2018). Hydraulic fracturing volume is associated with induced earthquake productivity in the Duvernay play. *Science*, *359*, 304–308. doi: 10.1126/science.aao0159

Segall, P., Rubin, A. M., Bradley, M., & Rice, J. R. (2010). Dilatant strengthening as a mechanism for slow slip events. *J. Geophys. Res.,*, *115*(B12305). doi: 10.1029/2010JB007449

Shipton, Z. K., & Cowie, P. A. (2001). Damage zone and slip surface evolution over μm to km scales in high-porosity Navajo sandstone, Utah. *Journal of Structural Geology*, *23*, 1825-1844.

Toda, S., Stein, R. S., Sevilgen, V., & Lin, J. (2011). *Coulomb 3.3 graphic-rich deformation and stress-change software for earthquake, tectonic, and volcano research and teaching-user guide* (Tech. Rep.). US Geological Survey.

Trudgill, B., & Cartwright, J. (1994). Relay-ramp forms and normal-fault linkages, Canyonlands National Park, Utah. *Geological Society of America Bulletin*, *106*(9), 1143–1157.

Trugman, D. T., & Shearer, P. M. (2017). Growclust: A hierarchical clustering algorithm for relative earthquake relocation, with application to the Spanish Springs and Sheldon, Nevada, earthquake sequences. *Seismological Research Letters*, *88*(2A), 379–391.

Waldhauser, F., & Ellsworth, W. L. (2000). A double-difference earthquake location algorithm: Method and application to the northern Hayward fault, California. *Bulletin of the Seismological Society of America*, *90*(6), 1353–1368.

Wang, B., Harrington, R. M., Liu, Y., Kao, H., & Yu, H. (2019). Remote dynamic triggering of earthquakes in three unconventional canadian hydrocarbon regions based on a multiple-station matched-filter approach. *Bulletin of the Seismological Society of America*, *109*(1), 372–386.

Wang, B., Harrington, R. M., Liu, Y., Yu, H., Carey, A., & van der Elst, N. (2015). Isolated cases of remote dynamic triggering in Canada detected using cataloged earthquakes combined with a matched-filter approach. *Geophysical Research Letters*, *42*. doi: 10.1002/2015GL064377

Yu, H., Harrington, R., Liu, Y., & Wang, B. (2019). Induced seismicity driven by fluid diffusion revealed by a near-field hydraulic stimulation monitoring array in the Montney Basin, British Columbia. *Journal of Geophysical Research: Solid Earth*, *124*(5), 4694–4709.

Zhang, H., Eaton, D. W., Li, G., Liu, Y., & Harrington, R. M. (2016). Discriminating induced seismicity from natural earthquakes using moment tensors and source spectra. *Journal of Geophysical Research: Solid Earth*, *121*(2), 972-993. doi: 10.1002/2015jb012603